THE EUROPEAN
PHYSICAL JOURNAL C

Regular Article - Theoretical Physics

Dark matter in a charged variant of the Scotogenic model

Valentina De Romeri[1,a], **Miguel Puerta**[1,b], **Avelino Vicente**[1,2,c]

[1] Instituto de Física Corpuscular, CSIC-Universitat de València, 46980 Paterna, Spain
[2] Departament de Física Teòrica, Universitat de València, 46100 Burjassot, Spain

Abstract Scotogenic models are among the most popular possibilities to link dark matter and neutrino masses. In this work we discuss a variant of the Scotogenic model that includes charged fermions and a doublet with hypercharge 3/2. Neutrino masses are induced at the one-loop level thanks to the states belonging to the dark sector. However, in contrast to the standard Scotogenic model, only the scalar dark matter candidate is viable in this version. After presenting the model and explaining some particularities about neutrino mass generation, we concentrate on its dark matter phenomenology. We show that the observed dark matter relic density can be correctly reproduced in the usual parameter space regions found for the standard Scotogenic model or the Inert Doublet model. In addition, the presence of the charged fermions opens up new viable regions, not present in the original scenarios, provided some tuning of the parameters is allowed.

1 Introduction

The Standard Model (SM) of particle physics fails to address two of the most important open questions in current fundamental physics: the origin of neutrino masses and the nature of dark matter (DM). While these two issues might be completely independent, and the explanation to the DM puzzle might even come from a completely different branch of physics, it is tempting to explore extensions of the SM in which they are simultaneously addressed.

Many radiative neutrino mass models are good examples of such extensions. In this class of models, pioneered in [1–4], neutrino masses vanish at tree-level but become non-zero once loop corrections are included. This naturally explains the smallness of neutrino masses, which get suppressed by the usual loop factors. In many cases, they are induced at

one-loop, but there are many well-known examples leading to neutrino masses at higher loop orders, see [5] for a review. A symmetry is often introduced to avoid the generation of neutrino masses at tree-level. Interestingly, the lightest state charged under this symmetry becomes completely stable and hence can be a viable DM candidate [6], provided it has the correct quantum numbers [7].

One of the most popular models with this feature is the so-called Scotogenic model [8]. This economical setup extends the SM particle content with three singlet fermions and one *inert* scalar doublet, all odd under a $\mathbb{Z}_2$ parity. Neutrino masses are induced at the one-loop level and the lightest $\mathbb{Z}_2$-odd particle, which might be a fermion or a scalar state, becomes stable and can play the role of DM candidate. Both possibilities have been studied in detail and shown to be valid options. The fermion DM candidate can be produced in the early Universe via its Yukawa interactions. Although the bounds from lepton flavor violating (LFV) processes [9] strongly limit the allowed parameter space in this case, the observed DM relic density can be achieved [10] (see also [11–14]). Qualitatively similar conclusions were recently found in a variant of the Scotogenic model with Dirac fermion DM [15]. The scalar DM candidate does not suffer from this limitation since it can be produced via gauge and/or scalar interactions. In this case the DM phenomenology resembles that of the Inert Doublet model [16–20].

While the original Scotogenic model is a very attractive and economical setup, it is also interesting to consider variations with a richer phenomenology.[1] For instance, a simple extension including both singlet and triplet fermions [23] already leads to novel phenomenological signatures [24,25]. In this work we consider a variant of the Scotogenic model originally introduced in [26]. In addition to the usual inert doublet, in this case one introduces charged fermions and a

[a] e-mail: deromeri@ific.uv.es

[b] e-mail: miguel.puerta@ific.uv.es (corresponding author)

[c] e-mail: avelino.vicente@ific.uv.es

---

[1] The Scotogenic model can be generalized in many different ways, see [21] and references therein. Furthermore, the Scotogenic mechanism can be used to induce a small one-loop mass for a light DM candidate [22].

doublet with hypercharge 3/2. As a consequence, the particle spectrum contains many new charged states, including a doubly-charged scalar. The presence of these states naturally leads to a much richer collider phenomenology [26,27]. The aim of our work is to explore the DM phenomenology of the model, something that is done for the first time here. In contrast to the minimal Scotogenic model, only the scalar dark matter candidate is viable in this version, since the rest of the $\mathbb{Z}_2$-odd states are electrically charged. We will show that the observed DM relic density can be correctly reproduced in this model and identify the regions of the parameter space where this is achieved. In particular, we will demonstrate the existence of novel parameter regions, not present in the standard Scotogenic scenario, viable thanks to the electrically charged fermions in this model.

The rest of the manuscript is organized as follows. The model is introduced in Sect. 2, where detailed discussions on the scalar sector, the neutrino mass generation mechanism and the DM candidate can be found. Section 3 describes the approach followed in our numerical analysis. This Section also discusses the most relevant experimental bounds in our setup. Our results are given in Sect. 4, whereas a summary with the main conclusions derived from our work is given in Sect. 5. Finally, additional details are given in Appendices A and B.

2 The model

We consider the variant of the original Scotogenic model introduced in [26]. The SM particle content is extended by adding two $SU(2)_L$ doublets, η and Φ, with hypercharge 1/2 and 3/2, respectively, and two pairs of singlet vector-like fermions $\psi_{L,R}^a$ ($a = 1, 2$) with hypercharge -1. The scalar doublets of the model can be decomposed into $SU(2)_L$ components as

$$H = \begin{pmatrix} H^+ \\ H^0 \end{pmatrix}, \quad \eta = \begin{pmatrix} \eta^+ \\ \eta^0 \end{pmatrix}, \quad \Phi = \begin{pmatrix} \Phi^{++} \\ \Phi^+ \end{pmatrix}. \quad (1)$$

Here H is the usual SM Higgs doublet. As in the Scotogenic model, we impose an exact $\mathbb{Z}_2$ parity. All the new particles are odd under this symmetry, while the SM particles are assumed to be even. The particle content of the model is summarized in Table 1. We note that H and η are only distinguished by their $\mathbb{Z}_2$ charges. In fact, the scalar doublet η has the same quantum numbers as the usual inert doublet present in the Inert Scalar Doublet model [16] and the Scotogenic model [8].

The most general Yukawa Lagrangian involving the new particles can be written as

$$\mathcal{L}_Y = M_\psi \, \overline{\psi}_L \, \psi_R + Y^L \, \overline{\ell_L^c} \, \Phi \, \psi_L + Y^R \, \overline{\ell_L} \, \eta \, \psi_R + \text{h.c.}, \quad (2)$$

Table 1 Particle content of the model. q_L, ℓ_L, u_R, d_R, e_R and H are the usual SM fields

	q_L	u_R	d_R	ℓ_L	e_R	ψ_L	ψ_R	H	η	Φ
$SU(3)_C$	**3**	$\bar{\mathbf{3}}$	$\bar{\mathbf{3}}$	**1**	**1**	**1**	**1**	**1**	**1**	**1**
$SU(2)_L$	**2**	**1**	**1**	**2**	**1**	**1**	**1**	**2**	**2**	**2**
$U(1)_Y$	$\frac{1}{6}$	$\frac{2}{3}$	$-\frac{1}{3}$	$-\frac{1}{2}$	-1	-1	-1	$\frac{1}{2}$	$\frac{1}{2}$	$\frac{3}{2}$
$\mathbf{Z}_2$	$+$	$+$	$+$	$+$	$+$	$-$	$-$	$+$	$-$	$-$
GENERATIONS	3	3	3	3	3	2	2	1	1	1

where M_ψ is a 2×2 vector-like (Dirac) mass matrix, which we take to be diagonal without loss of generality, while Y^L and Y^R are dimensionless 3×2 complex matrices. The most general scalar potential is given by

$$\mathcal{V} = \mu_1^2 \, |H|^2 + \mu_2^2 \, |\eta|^2 + \mu_\Phi^2 \, |\Phi|^2 + \frac{1}{2} \, \lambda_1 \, |H|^4$$

$$+ \frac{1}{2} \, \lambda_2 \, |\eta|^4 + \frac{1}{2} \, \lambda_\Phi \, |\Phi|^4$$

$$+ \lambda_3 \, |H|^2 \, |\eta|^2 + \lambda_4 \, |H^\dagger \eta|^2$$

$$+ \rho_1 \, |H|^2 \, |\Phi|^2 + \rho_2 \, |\eta|^2 \, |\Phi|^2$$

$$+ \sigma_1 \, |H^\dagger \Phi|^2 + \sigma_2 \, |\eta^\dagger \Phi|^2$$

$$+ \frac{1}{2} \left[\lambda_5 \, (H^\dagger \eta)^2 + \text{h.c.} \right]$$

$$+ \left[\kappa \, (\Phi^\dagger H)(\eta H) + \text{h.c.} \right], \quad (3)$$

where μ_1, μ_2 and μ_Φ are parameters with dimension of mass and λ_j ($j = 1, 2, 3, 4, 5$), λ_Φ, ρ_1, ρ_2, σ_1, σ_2 and κ are dimensionless. We note that in the presence of a non-zero κ term it is not possible to define a conserved lepton number. As shown below, this plays a crucial role for the generation of neutrino masses.
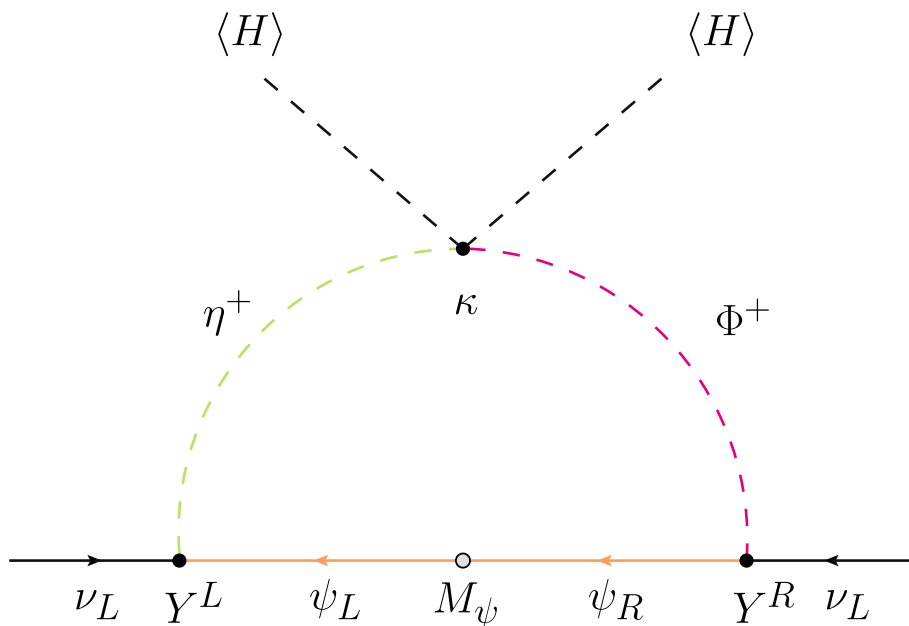
2.1 Scalar sector

Let us now discuss the resulting scalar particle content of the model. We will assume a minimum of the potential characterized by the vacuum expectation values (VEVs)

$$\langle H \rangle = \frac{1}{\sqrt{2}} \begin{pmatrix} 0 \\ v \end{pmatrix}, \quad \langle \eta \rangle = 0, \quad \langle \Phi \rangle = 0, \quad (4)$$

with $v \simeq 246$ GeV the usual SM VEV. This vacuum preserves the $\mathbb{Z}_2$ parity, which remains unbroken after electroweak symmetry breaking. This forbids the mixing between H, even under $\mathbb{Z}_2$, and the η and Φ doublets, odd under $\mathbb{Z}_2$. The neutral H^0 and η^0 states can be split into their CP-even and CP-odd components as

$$H^0 = \frac{1}{\sqrt{2}} \, (h + i \, A + v), \quad (5)$$

Fig. 1 One-loop diagram which generates neutrino masses in the variant of the Scotogenic model under consideration. Due to electric charge conservation, in each vertex the relevant components of η and Φ are the singly-charged ones

$$\eta^0 = \frac{1}{\sqrt{2}} (\eta_R + i\,\eta_I). \tag{6}$$

The CP-even state h can be identified with the SM Higgs boson, with $m_h \approx 125$ GeV, while A is the Goldstone boson that becomes the longitudinal component of the Z boson. Assuming that CP is conserved in the scalar sector, η_R and η_I do not mix. Their masses are given by

$$m^2_{\eta_{R,I}} = \mu_2^2 + \frac{1}{2}(\lambda_3 + \lambda_4 \pm \lambda_5)\,v^2. \tag{7}$$

The charged component of H becomes the longitudinal component of the W boson. The charged component of η mixes with the singly-charged component of Φ. Their Lagrangian mass term can be written as

$$\mathcal{L}_m = \begin{pmatrix} \eta^- & \Phi^- \end{pmatrix} \begin{pmatrix} m^2_{\eta^\pm} & m^2_{12} \\ m^2_{12} & m^2_{\Phi^\pm} \end{pmatrix} \begin{pmatrix} \eta^+ \\ \Phi^+ \end{pmatrix} + \text{h.c.}, \tag{8}$$

with

$$m^2_{\eta^\pm} = \mu_2^2 + \frac{1}{2}\lambda_3\,v^2, \tag{9}$$

$$m^2_{\Phi^\pm} = \mu_\Phi^2 + \frac{1}{2}(\rho_1 + \sigma_1)\,v^2, \tag{10}$$

$$m^2_{12} = \frac{1}{2}\kappa\,v^2. \tag{11}$$

The gauge eigenstates η^+ and Φ^+ are related to the mass eigenstates H_1^+ and H_2^+ as

$$\begin{pmatrix} H_1^+ \\ H_2^+ \end{pmatrix} = \begin{pmatrix} c_\chi & s_\chi \\ -s_\chi & c_\chi \end{pmatrix} \begin{pmatrix} \eta^+ \\ \Phi^+ \end{pmatrix}, \tag{12}$$

where $c_\chi = \cos\chi$, $s_\chi = \sin\chi$ and χ is a mixing angle. The Lagrangian mass term can be written in terms of the mass

eigenstates H_1^+ and H_2^+ as

$$\mathcal{L}_m = \begin{pmatrix} H_1^- & H_2^- \end{pmatrix} \begin{pmatrix} m_{H_1^\pm} & 0 \\ 0 & m_{H_2^\pm} \end{pmatrix} \begin{pmatrix} H_1^+ \\ H_2^+ \end{pmatrix} + \text{h.c.}. \tag{13}$$

This allows us to obtain the mixing angle χ. Combining Eqs. (8) and (13) with Eq. (12) one finds

$$c_\chi\,s_\chi = \frac{m^2_{H_1^\pm} - m^2_{H_2^\pm}}{\left[\frac{(m^2_{\Phi^\pm} - m^2_{\eta^\pm})^2}{m^2_{12}} + 4\,m^2_{12} \right]}$$

$$\approx \frac{m^2_{12}}{m^2_{H_1^\pm} - m^2_{H_2^\pm}} = \frac{\kappa\,v^2}{2\,(m^2_{H_1^\pm} - m^2_{H_2^\pm})}, \tag{14}$$

where in the second step we have assumed χ to be a small mixing angle or, equivalently, $\kappa \ll 1$. Finally, the mass of the doubly-charged Φ^{++} is given by

$$m^2_{\Phi^{++}} = \mu_\Phi^2 + \frac{1}{2}\rho_1\,v^2. \tag{15}$$

2.2 Neutrino mass generation

In this model, neutrino masses are induced at the one-loop level by the diagram in Fig. 1.[2] The $\mathbb{Z}_2$-odd states in the loop are electrically charged, in contrast to the original Scotogenic model, which has electrically neutral states running in the loop. The resulting neutrino mass matrix can be easily computed with the general expressions in Appendix A. In this model, $n_S = n_F = 2$, with $S \equiv \{H_1^\pm, H_2^\pm\}$ and $F \equiv \{\psi_1, \psi_2\}$. The masses of the scalars in the loop are $m^2_{H_1^\pm}$ and $m^2_{H_2^\pm}$, defined in Eq. (13), whereas the masses of the

---

[2] All Feynman diagrams in our paper were made with `JaxoDraw` [28,29].

fermions are m_{ψ^1} and m_{ψ^2}, with m_{ψ^b} ($b = 1, 2$) the diagonal components of the matrix M_ψ, introduced in Eq. (2). One can also read the couplings of $H_1^\pm$ and $H_2^\pm$ from Eqs. (2) and (12), obtaining

$$Y_{H_1^\pm}^L \equiv Y^L s_\chi, \quad Y_{H_1^\pm}^R \equiv Y^L c_\chi, \qquad (16)$$

$$Y_{H_2^\pm}^L \equiv Y^R c_\chi, \quad Y_{H_2^\pm}^R \equiv -Y^R s_\chi. \qquad (17)$$

Therefore, the contribution to $(m_\nu)_{\alpha\beta}$ of the diagram displayed in Fig. 1 is proportional to $Y_{\alpha b}^L Y_{\beta b}^R$, with b the fermion index. It is easy to realize that there is a *mirror* contribution proportional to $Y_{\beta b}^L Y_{\alpha b}^R$, obtained after exchanging the scalars. In summary, the neutrino mass matrix can be written as

$$(m_\nu)_{\alpha\beta} = \sum_{b=1}^2 \left[(m_\nu)_{\alpha\beta}^{\{H_1^\pm, \psi^b\}} + (m_\nu)_{\alpha\beta}^{\{H_2^\pm, \psi^b\}} \right], \qquad (18)$$

with

$$(m_\nu)_{\alpha\beta}^{\{H_1^\pm, \psi^b\}} = \frac{Y_{\alpha b}^L Y_{\beta b}^R + Y_{\alpha b}^R Y_{\beta b}^L}{16\pi^2} s_\chi c_\chi m_{\psi^b}$$
$$\times \left[\Delta_\epsilon + 1 - \frac{m_{\psi^b}^2 \log m_{\psi^b}^2 - m_{H_1^\pm}^2 \log m_{H_1^\pm}^2}{m_{\psi^b}^2 - m_{H_1^\pm}^2} \right], \quad (19)$$

$$(m_\nu)_{\alpha\beta}^{\{H_2^\pm, \psi^b\}} = -\frac{Y_{\alpha b}^L Y_{\beta b}^R + Y_{\alpha b}^R Y_{\beta b}^L}{16\pi^2} s_\chi c_\chi m_{\psi^b}$$
$$\times \left[\Delta_\epsilon + 1 - \frac{m_{\psi^b}^2 \log m_{\psi^b}^2 - m_{H_2^\pm}^2 \log m_{H_2^\pm}^2}{m_{\psi^b}^2 - m_{H_2^\pm}^2} \right]. \quad (20)$$

The addition of both contributions cancels out the divergence (Δ_ϵ), as expected. We can finally use Eq. (14) to replace the mixing angle χ in Eqs. (19) and (20). By doing this, and also by assuming the hierarchy $m_{H_1^\pm}^2, m_{H_2^\pm}^2 \ll m_{\psi^b}^2$, one finds

$$(m_\nu)_{\alpha\beta} = \sum_{b=1}^2 \frac{Y_{\alpha b}^L Y_{\beta b}^R + Y_{\alpha b}^R Y_{\beta b}^L}{32\pi^2 m_{\psi^a}} \frac{\kappa v^2}{m_{H_2^\pm}^2 - m_{H_1^\pm}^2}$$
$$\times \left(m_{H_2^\pm}^2 \log \frac{m_{\psi^b}^2}{m_{H_2^\pm}^2} - m_{H_1^\pm}^2 \log \frac{m_{\psi^b}^2}{m_{H_1^\pm}^2} \right). \qquad (21)$$

This expression matches the result in [26]. Neutrino masses are proportional to the κ parameter, as expected from symmetry arguments. In the limit $\kappa \to 0$ lepton number is restored, and this explains that Majorana neutrino masses can only be induced with $\kappa \neq 0$. Furthermore, $\kappa \ll 1$ is natural, in the sense of 't Hooft [30]. As in the Scotogenic model, small neutrino masses can be naturally generated in this model. One can generate $m_\nu \sim 1$ eV with $Y^{R,L} \sim 1$, $m_{H_1^\pm} \sim 300$ GeV, $m_{H_2^\pm} \sim 400$ GeV and $m_{\psi^a} \sim 1$ TeV if $\kappa \sim 10^{-12}$.

Table 2 Values of the input parameters considered in the numerical scan

$\lambda_1 = 0.26$	$m_{\psi^1} = 2.1$ TeV
$\lambda_2 = 0.5$	$m_{\psi^2} = 2.3$ TeV
$\lambda_3 = 10^{-2}$	$\rho_1 = 0.5$
$\lambda_4 \in [-0.5, -10^{-4}]$	$\rho_2 = 0.7$
$\lambda_5 \in [-0.32, -0.003]$	$\sigma_1 \in [10^{-5}, 0.16]$
$\lambda_\Phi = 3 \times 10^{-3}$	$\sigma_2 = 10^{-2}$
$\mu_\Phi^2 \in [100, 4.4 \times 10^6]$ GeV^2	$\kappa = 10^{-8}$
$\mu_2^2 = \mu_\Phi^2$ except if $m_{\eta_R} \in [50, 100]$ GeV	

2.3 Dark matter candidate

As a consequence of the conservation of the $\mathbb{Z}_2$ parity, the lightest $\mathbb{Z}_2$-odd state is stable and cannot decay. In contrast to the Scotogenic model, the only potentially viable candidate is one of the neutral η scalars, either η_R or η_I, since the other $\mathbb{Z}_2$-odd states are electrically charged. Their mass difference is controlled by the λ_5 quartic coupling, as shown in Eq. (7),

$$m_{\eta_R}^2 - m_{\eta_I}^2 = \lambda_5 v^2. \qquad (22)$$

Another difference with respect to the Scotogenic model is that this mass difference can in principle be large. This is because the λ_5 coupling does not enter the neutrino mass formula, see Eq. (21), and can be $\sim \mathcal{O}(1)$. Also, we note that the sign of λ_5 determines the DM candidate. η_I is the DM candidate if $\lambda_5 > 0$, while $\lambda_5 < 0$ selects η_R as the DM candidate.

The η_R and η_I fields couple to the electroweak gauge bosons, since they originate from an $SU(2)_L$ doublet with hypercharge 1/2. Their production in the early Universe is thus expected to be generally dominated by gauge interactions. The exception to this rule will be found when the mass of the DM candidate is close to $\sim m_h/2$, when the so-called Higgs portal will be the most important channel. In general, the DM phenomenology of the model is expected to be similar to that of the Inert Scalar Doublet model [16], a popular and economical model for DM [17,18]. Finally, we point out that the DM candidates, η_R and η_I, carry the quantum numbers of a supersymmetric sneutrino, except for lepton number.

3 Analysis and experimental bounds

We now proceed to discuss the approach followed in our numerical analysis and the experimental bounds considered. The first step has been the implementation of the model in SARAH (version 4.11.0) [31], a Mathematica

package for the analytical evaluation of the model.[3] With the help of this tool, we have created a `SPheno (version 4.0.2)` [33,34] module with the required numerical routines to obtain the particle spectrum and compute several observables of interest in our model. This includes the calculation of flavor violation observables with `FlavorKit` [35]. Finally, we have used `micrOmegas (version 5.0.9)` [36] for the evaluation of DM observables, such as the DM relic density and direct and indirect detection predictions. We performed a numerical scan with ~ 10000 points. Our choice of parameters is summarized in Table 2. In particular, we choose the negative sign for λ_5 so that throughout our analysis η_R plays the role of the dark matter. Let us recall that this is a choice just for definiteness, equivalent results would be obtained by assuming η_I as the lightest $\mathbb{Z}_2$-odd state. Furthermore, we take $\mu_2^2 = \mu_\Phi^2$ in most of the parameter space to guarantee that η_R (and not one of the charged states from Φ) is the lightest $\mathbb{Z}_2$-odd particle. An analogous reason lies behind the range chosen for μ_Φ^2.

The new particles introduced in this variant of the Scotogenic model may lead to different experimental signatures and affect the SM prediction of several observables. For this reason and throughout our analysis we have considered a list of experimental constraints.

Neutrino oscillation data The generation and smallness of neutrino masses is one of the main motivations behind the idea of Scotogenic models. In our analysis, we demand compatibility of the neutrino oscillation parameters with the most recent neutrino oscillation global fit [37]. This is achieved by adjusting the entries of the Yukawa matrices Y^L and Y^R by means of the master parametrization [38,39], which allows one to write

$$\left(Y^L\right)^T = \frac{1}{\sqrt{2 f}} \, \Sigma^{-1/2} \, W \, A \, \bar{D}_{\sqrt{m}} \, U^\dagger, \tag{23}$$

$$\left(Y^R\right)^T = \frac{1}{\sqrt{2 f}} \, \Sigma^{-1/2} \, W^* \, B \, \bar{D}_{\sqrt{m}} \, U^\dagger, \tag{24}$$

where Σ is a diagonal 2×2 matrix containing the positive singular values of the matrix M, with $M_{ij} = \omega_i \, \delta_{ij}$ and

$$\omega_i = \frac{1}{m_{\psi^i}} \left(m_{H_2^\pm}^2 \, \log \frac{m_{\psi^i}^2}{m_{H_2^\pm}^2} - m_{H_1^\pm}^2 \, \log \frac{m_{\psi^i}^2}{m_{H_1^\pm}^2} \right). \tag{25}$$

Moreover,

$$f = \frac{\kappa \, v^2}{32 \, \pi^2 \, (m_{H_2^\pm}^2 - m_{H_1^\pm}^2)} \tag{26}$$

is a global factor, U is the leptonic mixing matrix, a unitary 3×3 matrix that brings the neutrino mass matrix to a diagonal

form as

$$U^T \, m_\nu \, U = \text{diag}(m_1, m_2, m_3), \tag{27}$$

while the matrix $\bar{D}_{\sqrt{m}}$ is defined as

$$\bar{D}_{\sqrt{m}} = \begin{cases} \text{diag} \left(\sqrt{m_1}, \sqrt{m_2}, \sqrt{m_3}\right) & \text{if } m_1 \neq 0, \\ P \cdot \text{diag} \left(\sqrt{v}, \sqrt{m_2}, \sqrt{m_3}\right) \cdot P & \text{if } m_1 = 0. \end{cases} \tag{28}$$

Here v can actually be replaced by any arbitrary scale and P depends on the neutrino mass hierarchy. In case of normal ordering, P is just the identity matrix, while for inverted ordering P is a permutation matrix that exchanges the first and third elements. Finally, the matrices W, A and B are defined in Appendix B, where explicit analytical results for the elements of the Y^L and Y^R matrices are also given. In our numerical analysis we assume a normal mass ordering for light active neutrino masses and take vanishing CP violating phases for simplicity. We also assume that the lightest neutrino is massless.

Lepton flavor violation While this model could in principle produce signals at facilities looking for LFV processes, these have not been observed yet. Hence we can use current null searches for LFV to constrain the parameters of the model, in particular κ which determines the magnitude of the Yukawa matrices Y^L and Y^R. We consider the following most stringent bounds on rare LFV processes: BR($\mu \rightarrow e\gamma$) $< 4.2 \times 10^{-13}$ [40], BR($\mu \rightarrow eee$) $< 1. \times 10^{-12}$ [41] and CR(μ^-, Au $\rightarrow e^-$, Au) $< 7 \times 10^{-13}$ [42].

Electroweak precision observables The experimental accuracy of electroweak observables can be sensitive to the presence of new particles, like those introduced in this model. The main contribution to the higher-order calculation of electroweak precision observables is parameterized via the $\delta\rho$ parameter. We require an adequately small deviation of the ρ parameter from one through the following prescription: $-0.00022 \lesssim \delta\rho \lesssim 0.00098$ [43] (3σ range).

Dark matter searches We assume our DM candidate η_R to be in thermal equilibrium with the SM particles in the early Universe. We also assume a standard cosmological scenario. If no other dark matter candidates are present, then the relic abundance of η_R must be in agreement with the latest observations by the Planck satellite [44], which set a limit on the cosmological content of cold dark matter: $0.1164 \leq \Omega_{\eta_R} h^2 \leq 0.1236$ (3σ range). The relic abundance of η_R can also be subdominant, i.e. $\Omega_{\eta_R} h^2 < 0.1164$, however in this case another DM candidate is required to explain the totality of the cosmological dark matter. Moreover, η_R can be probed at dark matter experiments like direct detection facilities. We apply the most stringent bound on the WIMP-nucleon spin-independent (SI) elastic scatter cross-section from the XENON1T experiment [45]. We compute the direct detection cross section at tree-level. Since a more

---

[3] See [32] for a pedagogical introduction to the use of `SARAH`.

exhaustive study of this observable is out of the scope of this paper, we have considered the constraint

$$\frac{1}{2}|\lambda_3 + \lambda_4 + \lambda_5| \geq 10^{-3}, \tag{29}$$

obtained for the inert Higgs doublet [46] in order to avoid sizable loop corrections. If η_R annihilates into SM particles with a cross section typical of WIMPs, it may also be detected indirectly. We consider both γ rays and antiprotons as annihilation products and compare with the respective current bounds on the WIMP annihilation cross section set by the Fermi Large Area Telescope (LAT) satellite [47], the ground-based arrays of Cherenkov telescopes H.E.S.S. [48] and the Alpha Magnetic Spectrometer (AMS-02) [49–51] onboard the International Space Station.

LHC searches The new charged particles in the model can be copiously produced and detected at the LHC, see [26,27]. It is however beyond the scope of this work to perform a detailed collider study of the model. In order to guarantee compatibility with the current bounds, we have chosen $m_{\psi^{1,2}} > 1$ TeV in our numerical scan. The singly-charged scalars $H_{1,2}^+$ have masses in a wide range of values, always in the hundreds of GeV. Finally, the doubly-charged scalar Φ^{++} is chosen to be always heavier than ~ 200 GeV by imposing $\mu_2^2 \neq \mu_\Phi^2$ in the region $m_{\eta_R} \in [50$ GeV, 100 GeV]. This may seem as too little restrictive, since the currently most stringent bounds on a doubly-charged scalar range from 220 GeV [52] (for a Φ^{++} that decays into $W^+ W^+$) to 846 GeV [53] (for a Φ^{++} that decays into $\mu^+ \mu^+$). However, notice that in our model Φ^{++} is $\mathbb{Z}_2$-odd and its decays always include DM particles. In fact, we have found that in many parameter points Φ^{++} decays as $\Phi^{++} \rightarrow H_1^+ W^+$, followed by $H_1^+ \rightarrow \eta_R \ell^+ \nu$, thus leading to large amounts of missing energy in the final state.

Invisible decay width of the Higgs boson If the new neutral scalars η_R and η_I are light enough, new invisible decay channels of the Higgs boson will be kinematically accessible. We require that their contribution to the invisible decay width of the Higgs boson is not larger than the currently most stringent experimental bound: BR($h \rightarrow$ inv) $\lesssim 19\%$ [54]. Our computation of BR($h \rightarrow$ inv) includes the decay BR($h \rightarrow \eta_R \eta_R$), when kinematically possible, and also BR($h \rightarrow \eta_I \eta_I$) when $m_{\eta_I} - m_{\eta_R} < 10$ GeV. We estimate that for larger mass differences between η_I and η_R, η_I would decay visibly inside the detector. Moreover, the presence of charged scalars may also modify the Higgs photon coupling to two photons. For this reason we further impose that $0.84 \lesssim$ BR($h \rightarrow \gamma\gamma$)/BR($h \rightarrow \gamma\gamma$)$_{SM} \lesssim 1.41$, with BR($h \rightarrow \gamma\gamma$)$_{SM} = (0.227 \pm 0.011) \times 10^{-2}$ [43].

η_I lifetime Searches for long-lived particles at the LHC usually look for displaced vertices. In order to ensure compatibility with the non-observation of such signatures, we

Table 3 List of experimental constraints applied to the numerical scan

BR($\mu \rightarrow e\gamma$)	$< 4.2 \times 10^{-13}$ [40]
BR($\mu \rightarrow eee$)	$< 1. \times 10^{-12}$ [41]
CR(μ^-, Au $\rightarrow e^-$, Au)	$< 7 \times 10^{-13}$ [42]
$\frac{BR(h \rightarrow \gamma\gamma)}{BR(h \rightarrow \gamma\gamma)_{SM}}$	[0.84, 1.41] [43]
BR($h \rightarrow \gamma\gamma$)$_{SM}$	$(0.227 \pm 0.011) \times 10^{-2}$ [43]
BR($h \rightarrow$ inv)	0.19 [54]
$\delta\rho$	$[-0.00022, 0.00098]$ [43]
$\Omega_{\eta_R} h^2$	[0.1164, 0.1236] [43]

require $\tau(\eta_I) \ll 1$ s. This translates into the constraint $|\lambda_5| \geq 5 \times 10^{-4}$, which guarantees that η_I decays fast enough into η_R.

Theoretical considerations We require that the expansion of the scalar potential (see Eq. 3) around its minimum must be perturbatively valid. At this scope, we take all scalar quartic couplings to be $\lesssim 1$. Similarly, the elements of the Y^L and Y^R Yukawa matrices are also bounded to be $\lesssim 1$. Furthermore, all quartic couplings will take positive values in our numerical scans. While more sofisticated analyses are required in order to establish that the considered vacuum configuration is stable, in particular in what concerns the conservation of the $\mathbb{Z}_2$ parity (at the electroweak or at higher energy scales), they are clearly beyond the scope of our work. We refer to [21] for a detailed discussion of these issues.

We summarize in Table 3 the list of experimental constraints applied in the numerical scan.

4 Numerical results

In this section we summarize our results of the analysis of η_R as a dark matter candidate in the model. As we previously commented, this is the only potential DM candidate in this model, given the choice of negative sign of λ_5 (see Sect. 2.3). Figure 2 shows the expected η_R relic abundance as a function of the mass of η_R. Points colored in magenta denote solutions which can reproduce the observed cold dark matter relic density, as they fall within the 3σ range derived by the Planck satellite data [44], $\Omega_{\eta_R} h^2 = 0.120 \pm 0.0036$ (green band). From this analysis we can identify that the preferred DM mass range lies around 500 GeV $\lesssim m_{\eta_R} \lesssim 800$ GeV. Blue points also refer to allowed solutions but where η_R would be a subdominant component of dark matter, and another candidate would be required. Finally, gray points denote solutions excluded by any of the constraints previously discussed in Sect. 3. In particular, the Planck constraint itself rules out most of the solutions leading to excessively large relic density. Another large set of solutions with 70 GeV $\lesssim m_{\eta_R} \lesssim 700$ GeV is excluded by the current bound
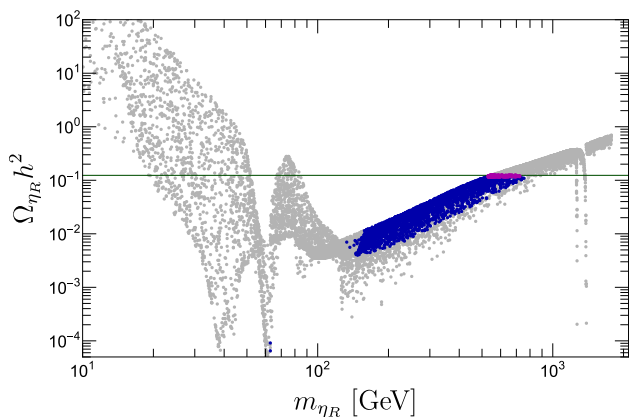
Fig. 2 Relic abundance of η_R as a function of m_{η_R}. Magenta points depict solutions in agreement with the cold dark matter measurement obtained from Planck data [44] (green band, 3σ interval). Blue points denote allowed solutions but leading to underabundant dark matter. Gray points are excluded by any of the constraints listed in Sect. 3

Fig. 3 Dominant diagram contributing to the co-annihilation channel $H_1^- H_2^+ \to \nu\nu$. Notice that both Yukawa matrices, Y^L and Y^R, must have sizable entries to make this process efficient

on WIMP-nucleon SI elastic scattering cross section set by the experiment XENON1T [45].

Looking at the figure from left to right, the first dip refers to the Z-pole, where $m_{\eta_R} \sim M_Z/2$ and annihilations via s-channel Z exchange are relevant. A similar feature appears at $m_{\eta_R} \sim 60$ GeV, where a narrower dip indicates efficient annihilations via s-channel Higgs exchange. However, most solutions with $m_{\eta_R} \lesssim 60$ GeV appear to be in conflict with current collider limits on BR($h \to$ inv) and with LHC searches for doubly-charged scalars and are therefore excluded. Notice that the s-channel Higgs annihilations are in general more efficient than the Z-mediated ones, not being momentum suppressed, and in principle could lead to solutions with $\Omega_{\eta_R} h^2 < 10^{-5}$. Only very few solutions eventually survive in the Higgs-pole region at $m_{\eta_R} \lesssim 100$ GeV, due to a variety of constraints, among which BR($h \to \gamma\gamma$) and BR($h \to$ inv) are the most important ones. These parameter points have very small relic density. After the Higgs pole, η_R quartic interactions with gauge bosons and heavy quarks become effective, when kinematically allowed. In particular, η_R annihilations into W^+W^- via quartic couplings are efficient at $m_{\eta_R} \gtrsim 80$ GeV, translating into a third drop in the relic abundance. As soon as kinematically allowed, η_R can then annihilate also into two Higgs bosons. In general, for $m_{\eta_R} \gtrsim 100$ GeV, the η_R relic density increases as its annihilation cross section drops proportionally as $\sim \frac{1}{m_{\eta_R}^2}$.

A very interesting feature appears at $m_{\eta_R} \sim 1.3$ TeV. The relic density suddenly drops to very small values due to a very efficient co-annihilation channel $H_1^- H_2^+ \to \nu\nu$, mediated by the vector-like fermions $\psi_{1,2}$ in t-channel, as shown in Fig. 3. This contribution is made very efficient by the magnitude of the relevant entries of the Yukawa matrices entering the diagram. The same Yukawas also play a relevant role in the rare LFV process $\mu \to e\gamma$, which turns out to exceed
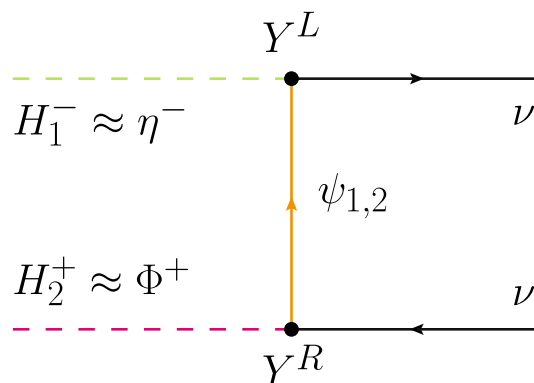
the current limit set by MEG [40] and thus excludes all solutions falling in this very narrow pole. Nonetheless, given the large freedom due to the vast array of parameters that can be varied in the parameterization of the Yukawa matrices (see Appendix B), one can always find a fine-tuned combination which allows to keep the co-annihilation channel $H_1^- H_2^+ \to \nu\nu$ efficient while at the same time not leading to a BR($\mu \to e\gamma$) in conflict with current observations. This can be seen in Fig. 4, where we show the dependence of BR($\mu \to e\gamma$) and $\Omega_{\eta_R} h^2$ as a function of the parameters K_{12} (left panel) and T_{12} (right panel). To obtain these figures we extracted one solution at $m_{\eta_R} \sim 1.3$ TeV from our general scan (see Fig. 2) – which we recall was made fixing $K_{12} = 0$ and $T_{12} = 0$ – and we scanned around those central values. Eventually, few allowed solutions (both with a relic abundance matching current observations and underabundant) will appear at $m_{\eta_R} \sim 1.3$ TeV. Let us point out that similar features with fine-tuned solutions may be present also in other parts of the parameter space. In particular, we notice that this feature depends on some of the parameters of the model (for example, the charged fermion masses). Therefore, one should be able to find it in other regions below (or above) 1.3 TeV with other parameter configurations.

Next we proceed to discuss the results for η_R direct detection.

In full generality, the tree-level SI η_R-nucleon interaction cross section receives two contributions, from scattering through the Higgs or Z bosons. However, since the λ_5 quartic coupling induces a mass splitting between η_R and η_I, eventually it turns out that the interaction through the Z boson is kinematically forbidden, or leads to inelastic scattering, in a large part of the parameter space. Should this not be the case, the η_R–nucleon interaction through the Z boson would dominate (since the η doublet has hypercharge different from zero) and very likely exceed the current bounds from DM direct detection experiments. We show in Fig. 5 the SI η_R–nucleon elastic scattering cross section, weighted by
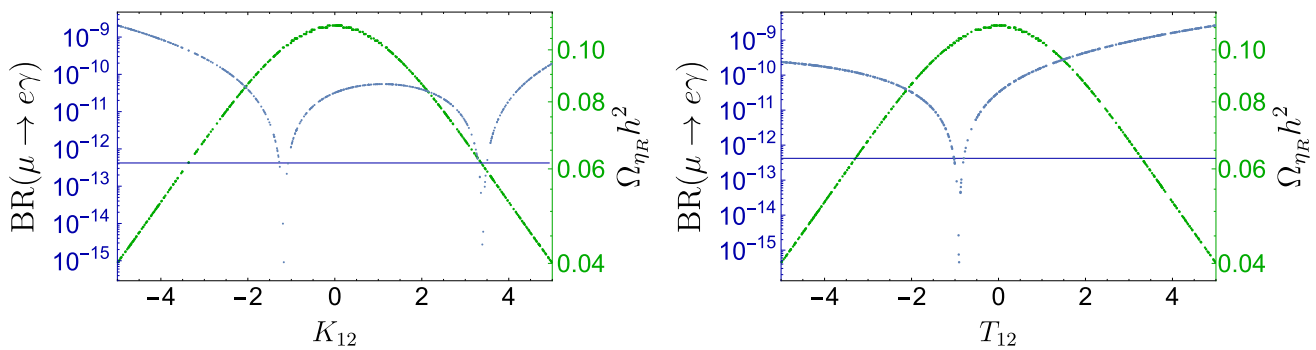
Fig. 4 BR($\mu \to e\gamma$) (left vertical axis, blue points) and relic abundance of η_R (right vertical axis, green points) as a function of K_{12} (left panel) and T_{12} (right panel). The horizontal line represents the current upper bound on BR($\mu \to e\gamma$) [40]. Therefore, all blue points above this line are excluded

Fig. 5 Spin-independent η_R-nucleon elastic scattering cross section – weighted by the relative abundance – versus m_{η_R}. Same color code as in Fig. 2. The green dashed area is excluded by the most recent upper bound from the XENON1T experiment [45]. The dashed orange curve indicates the expected discovery limit corresponding to the "ν-floor" from CEνNS of solar and atmospheric neutrinos for a Ge target [60]. The dashed red curve depicts the projected sensitivity expected at LUX-ZEPLIN (LZ) [61]
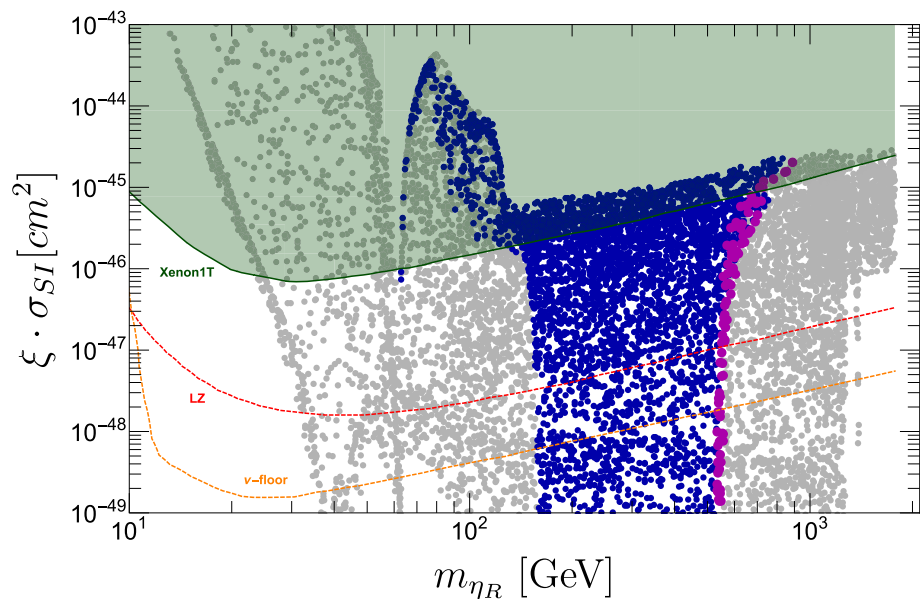
$\xi = \frac{\Omega_{\eta_R}}{\Omega_{\text{CDM,Planck}}}$ versus the η_R mass. We use the same color code as in Fig. 2. The plain green line and dashed area indicate the current most stringent limit from XENON1T [45]. Even if not shown here, other stringent constraints on the SI η_R-nucleon elastic scattering cross section apply from the liquid xenon experiments LUX [55,56] and PandaX-II [57]. Liquid argon experiments like DarkSide-50 [58] and DEAP-3600 [59] are instead presently limited and hence less constraining, due to lower exposures and the currently low acceptance in DEAP-3600. We also illustrate for comparison the expected discovery limit corresponding to the "ν-floor" from coherent elastic neutrino-nucleus scattering (CEνNS) for a Ge target [60] (dashed orange line), as well as the sensitivity projection (90% CL) for the future experiment LUX-ZEPLIN (LZ, red dashed) [61]. Other future experiments like XENONnT [62], DarkSide-20k [63], ARGO [63] and DARWIN [64,65] (see [66] for a recent review), not shown here not to overcrowd the figure, will in principle be able to explore the parameter space of this model. Given the current experimental constraints, most of the solutions with a relic abundance falling within the

3σ C.L. cold dark matter range obtained by the Planck collaboration [44] lie in a narrow region around $m_{\eta_R} \sim 500 - 700$ GeV. Many more solutions leading to under-abundant dark matter lie at ~ 150 GeV $\lesssim m_{\eta_R} \sim 500$ GeV and could be tested at future DD experiments. On the whole, the phenomenology of the scalar DM candidate in this model, while richer, shares similar properties to that of the analogous scalar DM candidates in the simple Scotogenic Model [8], in Inert Scalar Doublet models, and in other Scotogenic variants like the Singlet-Triplet Scotogenic model [25].

Another η_R search strategy is via its indirect detection. If it annihilates into SM particles or messengers (with sizable annihilation cross section, close to the thermal value) it can contribute to the flux of cosmic particles that reaches the Earth. Photons, and more specifically γ rays are among the most suitable messengers to probe WIMP dark matter indirectly. They are not deflected during propagation, so they carry information about their source, and they are relatively easy to detect. When η_R is lighter than M_W, only annihilations into fermions lighter than m_{η_R} are allowed at tree

level, with the heaviest kinematically allowed fermion final states dominating (i.e. $\eta_R\eta_R \rightarrow b\bar{b}$ and $\eta_R\eta_R \rightarrow \tau^+\tau^-$). At higher masses, when kinematically allowed through the corresponding quartic couplings, also the following channels open: $\eta_R\eta_R \rightarrow W^+W^-, hh, Z^0Z^0$. The hadronization of the gauge bosons, Higgs boson or quarks produces neutral pions, which in turn decay into photons thus giving rise to a γ-ray flux with a continuum spectrum which may be detected at indirect detection experiments. Besides this featureless γ-ray spectrum, the model also predicts a spectral feature from the internal bremsstrahlung process $\eta_R\eta_R \rightarrow W^+W^-\gamma$, similarly to the Inert Doublet model [67,68]. We include this contribution in our analysis.

While more challenging due to uncertainties in the treatment of their propagation, charged particles can also be used to probe for η_R annihilations. PAMELA [69,70] and, more recently, the AMS-02 [71,72] positrons data allow to place constraints on annihilating WIMPs, which are particularly stringent if they annihilate mainly to the first two generations of charged leptons. In our case, at $m_{\eta_R} < m_W$, η_R annihilates predominantly into τs (and $b\bar{b}$). Hence, bounds from cosmic positrons are less stringent than those from γ rays. On the other hand, AMS-02 data on the antiproton flux and the Boron to Carbon (B/C) ratio can be used to constrain the η_R annihilation cross section [49–51]. Provided that astrophysical uncertainties on the $\bar{p}$ production, propagation and on Solar modulation are reliably taken into account (see e.g.

[73–75]), these bounds result to be stronger than γ-ray limits from dwarf spheroidal satellite galaxies (dSphs) over a wide mass range.

We focus on the main η_R annihilation channels into $b\bar{b}$, $\tau^+\tau^-$ and W^+W^- to compare with current limits set by γ-ray observations of Milky Way dSphs with Fermi-LAT data [47], of the Galactic Center (GC) with the H.E.S.S. array of ground-based Cherenkov telescopes [48] and a combination of $\bar{p}$ and B/C data of AMS-02 [49,50]. Figure 6 shows the results of our numerical scan of the η_R annihilation cross section (weighted by ξ^2 and by the correspondent branching ratio) versus its mass, for the main annihilation channels: $\eta_R\eta_R \rightarrow b\bar{b}$ (green points), $\eta_R\eta_R \rightarrow \tau^+\tau^-$ (blue points) and $\eta_R\eta_R \rightarrow W^+W^-$ (dark red points). As in previous plots, gray points denote solutions excluded by any of the constraints listed in Sect. 3, while magenta points depict solutions in agreement with the cold dark matter measurement obtained from Planck data. In the same figure we depict the 95% C.L. upper limits currently set by the Fermi-LAT with γ-ray observations of Milky Way dSphs (6 years, Pass 8 event-level analysis) [47] (plain curves and shaded areas, assuming annihilation into $b\bar{b}$ (green), $\tau^+\tau^-$ (blue) and W^+W^- (dark red)). We also show the current upper limit obtained with data accumulated over 10 years by H.E.S.S. observations of the GC [48], assuming a W^+W^- annihilation channel and an Einasto dark matter density profile (dark red dot-dashed curve and shaded area). Current bounds from a combination
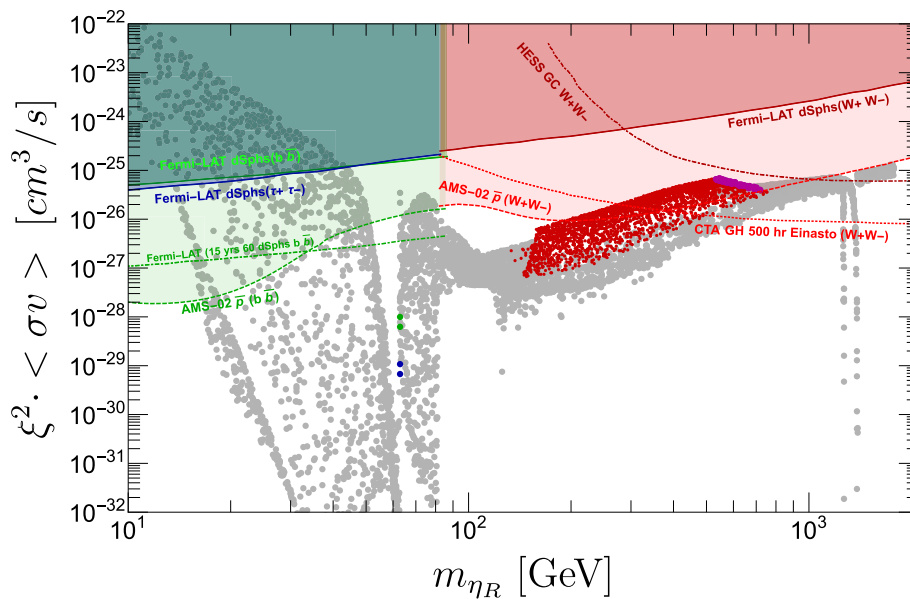

Fig. 6 η_R annihilation cross section for annihilations into $b\bar{b}$ (green), $\tau^+\tau^-$ (blue) and W^+W^- (magenta when η_R makes all the dark matter, red when it comprises a subdominant fraction) final states. The green, blue and red plain lines refer to the corresponding 95% C.L. upper limits currently set by Fermi-LAT γ-ray data from dSphs [47]. The dark red dot-dashed curve is the current 95% C.L. upper limit obtained by H.E.S.S. using GC data [48]. The green and red dashed lines denote current 95% C.L. constraints derived from the antiproton and B/C data of AMS-02 [50]. For comparison, we also show sensitivity projections for Fermi-LAT ($b\bar{b}$ channel, assuming 60 dSphs and 15 years of data) [76] and for CTA (looking at the galactic halo, W^+W^- channel) [77]

of $\bar{p}$ and B/C data of AMS-02 [49,50] are instead shown as dashed curves (green for $b\bar{b}$ and red for W^+W^- channels, respectively). As for comparison we further illustrate projected sensitivities for Fermi-LAT from a stacked analysis of 60 dSphs and 15 years of data, in the $b\bar{b}$ channel [76] (dot-dashed green line) and for the Cherenkov Telescope Array (CTA), for the Milky Way galactic halo target, assuming the W^+W^- annihilation channel and an Einasto dark matter density profile [77]. Our model predictions, not excluded by other constraints, lie at least a factor of few below current limits set by γ-ray observations with Fermi-LAT and H.E.S.S.. In particular, allowed solutions in the "low" (and narrow) mass window around $m_{\eta_R} \sim 60$ GeV ($b\bar{b}$ and $\tau^+\tau^-$ annihilation channels) are hardly found, so only a couple of them are shown for illustration. Predictions for these channels lie well below current bounds. Antiprotons and B/C data of AMS-02 instead already allow to exclude some solutions with 200 GeV $\lesssim m_{\eta_R} \lesssim 800$ GeV (W^+W^- annihilation channel), including the region of parameter space that could explain the totality of dark matter. We remark that these bounds are obtained under significant astrophysical uncertainties. Future telescopes like CTA as well as additional LAT data will allow to further explore these regions of the parameter space, thus allowing for multi-messenger indirect probes of this model. Finally let us comment that the annihilation cross section of non-relativistic η_R at the current epoch can be affected by a non-perturbative correction, the Sommerfeld enhancement [78–82] which would consequently affect also its indirect detection signatures. However, we did not include it in our calculation as a thorough treatment of this effect lies beyond the scope of this paper.

5 Conclusions

We have considered a variant of the Scotogenic model with an extended scalar content, in which one of the new doublets carries hypercharge $Y = 3/2$. As a consequence, the model particle spectrum contains new states, including a doubly-charged scalar, singly-charged scalars and new charged fermions leading to a rich collider phenomenology. Neutrino masses are generated radiatively as in other Scotogenic scenarios. However, contrarily to the simple Scotogenic model, in this setup only the lightest $\mathbb{Z}_2$-odd neutral scalar η is a viable dark matter candidate. We have considered η_R as the dark matter candidate and performed the first analysis of the dark matter phenomenology in this model. Our results show that the observed relic density can be obtained for η_R masses of 500 GeV $\lesssim m_{\eta_R} \lesssim 800$ GeV. This result is equivalent to that obtained in the Inert Doublet model and excludes scenarios with lighter dark matter candidates. In addition, we have found that the correct relic density can also be achieved at larger η_R masses if the coannihilation chan-

nel $H_1^- H_2^+ \to \nu\nu$ becomes efficient. However, this requires some fine-tuning to avoid the stringent constraints from lepton flavor violation. This feature is expected to appear in other regions of parameter space, thus enlarging the viable region for scalar dark matter in Scotogenic scenarios. Moreover, we have presented a full numerical analysis of the signatures expected at dark matter detection experiments, both via direct and indirect probes. We have found that most recent direct detection data from XENON1T already rule out a region of the parameter space in the mass range $m_{\eta_R} \sim 100$ GeV. Finally we have commented about indirect detection signatures with γ-rays and antiprotons data. While bounds derived with γ-ray data from Fermi-LAT and H.E.S.S. currently lie above the model predictions, AMS-02 antiproton data instead already allows to constrain some solutions in the 200 GeV $\lesssim m_{\eta_R} \lesssim 800$ GeV mass range, including the region in parameter space where η_R can account for all the dark matter.

Appendix A: Neutrino mass matrix in scotogenic models

In this Appendix we find a general analytical expression for one-loop contributions to the neutrino mass matrix in Scotogenic models. Let us consider a generic model with n_S scalars S_a with masses m_{Sa} ($a = 1, \ldots, n_S$) and n_F fermions F_b with masses m_{Fb} ($b = 1, \ldots, n_F$) that couple to light neutrinos with interaction terms of the form

$$\mathcal{L} = \left(Y_S^F \right)_{\alpha ab} \overline{\nu_{L\alpha}} \, S_a \, F_b + \text{h.c.}, \tag{30}$$

where Y_S^F is a $3 \times n_S \times n_F$ complex object. This interaction term induces neutrino masses at the one-loop level via the diagram in Fig. 7. The resulting neutrino mass matrix can be expressed as

$$i\,(m_\nu)_{\alpha\beta} = i \sum_{a,b} (m_\nu)_{\alpha\beta}^{\{S_a, F_b\}}. \qquad (31)$$

where the sum extends over all mass eigenstates running in the loop. Each $i\,(m_\nu)_{ij}^{\{S_a, F_b\}}$ represents the individual contribution by the scalar S_a and the fermion F_b and is given by

$$i\,(m_\nu)_{\alpha\beta}^{\{S_a, F_b\}} = (Y_S^F)_{\alpha ab}\,(Y_S^F)_{\beta ab} \int \frac{d^D k}{(2\pi)^D}$$
$$\times \frac{(\slashed{k} + m_{Fb})}{(k^2 - m_{Sa}^2)(k^2 - m_{Fb}^2)}, \qquad (32)$$

where $D = 4 - \varepsilon$ is the number of space-time dimensions, k is the momentum running in the loop and the external neutrinos have been taken at rest. The $\slashed{k}$ piece does not contribute since it is an odd function in k. The remaining term is logarithmically divergent. Introducing the usual Feynman's parameters, we can rewrite our expression as

$$i\,(m_\nu)_{\alpha\beta}^{\{S_a, F_b\}} = (Y_S^F)_{\alpha ab}\,(Y_S^F)_{\beta ab} \int_0^1 dx$$
$$\times \int \frac{d^D k}{(2\pi)^D} \frac{m_{Fb}}{(k^2 - C_{ab}^2)^2}, \qquad (33)$$

where $C_{ab}^2 = m_{Sa}^2 + m_{Fb}^2(1-x)$. One can now integrate in k and obtain

$$i\,(m_\nu)_{\alpha\beta}^{\{S_a, F_b\}} = \frac{i\,(Y_S^F)_{\alpha ab}\,(Y_S^F)_{\beta ab}}{16\pi^2} m_{Fb}$$
$$\times \int_0^1 dx \left[\Delta_\epsilon - \log C_{ab} + \mathcal{O}(\epsilon) \right], \qquad (34)$$

Fig. 7 Generic one-loop contribution to the neutrino mass matrix. F and S represent fermion and scalar mass eigenstates contributing to the neutrino mass matrix

where $\Delta_\epsilon = \frac{2}{\epsilon} - \gamma + \log 4\pi$ and γ is Euler's constant. Finally, we integrate in x and take the limit $\epsilon \to 0$ (which corresponds to $D \to 4$). This leads us to

$$(m_\nu)_{\alpha\beta}^{\{S_a, F_b\}}$$
$$= \frac{(Y_S^F)_{\alpha ab}\,(Y_S^F)_{\beta ab}}{16\pi^2} m_{Fb}$$
$$\times \left[\Delta_\epsilon + 1 - \frac{m_{Fb}^2 \log(m_{Fb}^2) - m_{Sa}^2 \log(m_{Sa}^2)}{m_{Fb}^2 - m_{Sa}^2} \right].$$
$$\qquad (35)$$

Equation (35) is our *master* expression for the one-loop contributions to the neutrino mass matrix. In order to compute the neutrino mass matrix in different versions of the Scotogenic model, one just needs to identify the scalar and fermion mass eigenstates running in the loop and replace the Y_S^F couplings by their expressions in terms of the model parameters. Then, summing over all individual contributions one finds the total one-loop neutrino mass matrix. We note that individual contributions to m_ν are divergent due to the Δ_ϵ term. However, the one-loop neutrino mass matrix is finite. Therefore, these divergences cancel out in the sum in Eq. (31).

As an example, we show this explicitly in the original Scotogenic model [8]. In this case one introduces the inert scalar doublet η, with the same definition as in the model in Sect. 2, as well as three generations of fermions N, singlets under the SM gauge group. The new N and η fields couple to the SM lepton doublet with the Yukawa term $Y^N \overline{\ell_L} \widetilde{\eta} N$, with $\widetilde{\eta} = i\tau_2 \eta^*$ and τ_2 the second Pauli matrix. Moreover, the neutral component of the η doublet can been split into its CP-even and CP-odd components as

$$\eta^0 = \frac{1}{\sqrt{2}} (\eta_R + i\,\eta_I). \qquad (36)$$
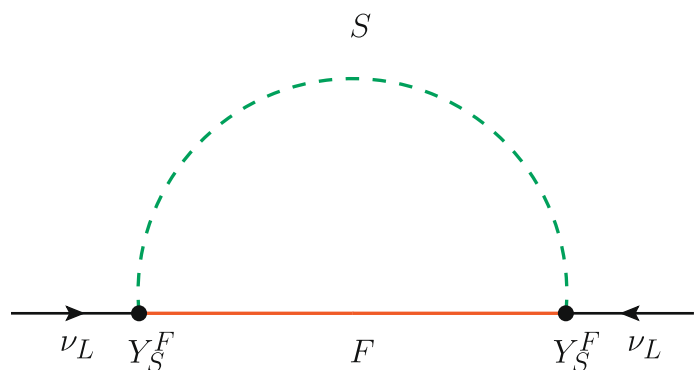
Assuming that CP is conserved in the scalar sector, η_R and η_I do not mix and constitute mass eigenstates. Therefore, in the Scotogenic model one has $n_S = 2$ and $n_F = 3$, with $S \equiv \{\eta_R, \eta_I\}$ and $F \equiv \{N_1, N_2, N_3\}$. Their couplings are given by

$$Y^{\eta_R} \equiv \frac{Y^N}{\sqrt{2}}, \quad Y^{\eta_I} \equiv i\frac{Y^N}{\sqrt{2}}. \tag{37}$$

Finally, applying Eq. (35) and summing over all the states in the loop we are able to obtain a finite expression (the divergences of the diagrams with η_R and η_I cancel each other) for the neutrino mass matrix

$$
\begin{aligned}
(m_\nu)_{\alpha\beta} &= \sum_{b=1}^{3} \frac{Y^N_{\alpha b} Y^N_{\beta b}}{32\pi^2} m_{Nb} \\
&\times \left[\frac{m^2_{\eta_R}}{m^2_{Nb} - m^2_{\eta_R}} \log\frac{m^2_{\eta_R}}{m^2_{Nb}} - \frac{m^2_{\eta_I}}{m^2_{Nb} - m^2_{\eta_I}} \log\frac{m^2_{\eta_I}}{m^2_{Nb}} \right],
\end{aligned}
\tag{38}
$$

where m_{η_R} and m_{η_I} are the corresponding masses for each component. This expression differs from the expression in [8] by a factor of $1/2$, an error that was first identified in v1 of [83].

Appendix B: General parametrization for the Yukawa matrices

The master parametrization [38,39] allows one to write the 3×2 Yukawa matrices Y^L and Y^R in terms of neutrino oscillation parameters as in Eqs. (23) and (24). In these expressions, W is a 2×2 unitary matrix, given in terms of the complex angle β as

$$W = \begin{pmatrix} \cos\beta & \sin\beta \\ -\sin\beta^* & \cos\beta^* \end{pmatrix}, \tag{39}$$

$A = T C_1$, with T a 2×2 upper-triangular matrix with positives real entries in the diagonal, and $B = (T^T)^{-1}(C_1 C_2 + K C_1)$, with K a 2×2 antisymmetric matrix, hence containing only one degree of freedom. The matrices C_1 and C_2 are given by

$$C_1 = \begin{pmatrix} z_1 & 0 & 0 \\ z_2 & 0 & 0 \end{pmatrix}, \quad C_2 = \begin{pmatrix} -1 & 0 & 0 \\ 0 & 1 & 0 \\ 0 & 0 & 1 \end{pmatrix}, \tag{40}$$

with z_1 and z_2 two complex numbers such that $z_1^2 + z_2^2 = 0$. With all these ingredients one can obtain explicit expressions for the elements of Y^L and Y^R, which will be determined from neutrino oscillation data as well as from a set of free parameters. We point out that these are the most general expressions for the elements of the Y^L and Y^R Yukawa matrices:

$$Y^L_{11} = \frac{c_{12}c_{13}\sqrt{m_1}(c_\beta(z_1 T_{11} + z_2 T_{12}) + z_2 T_{22}s_\beta) + c_{13}e^{-i\eta_2}\sqrt{m_2}s_{12}T_{11}c_\beta}{\sqrt{2f}\sqrt{\omega_1}} + \frac{\sqrt{m_3}s_{13}e^{i(\delta-\eta_3)}(T_{22}s_\beta + T_{12}c_\beta)}{\sqrt{2f}\sqrt{\omega_1}}, \tag{41}$$

$$
\begin{aligned}
Y^L_{21} &= -\frac{\sqrt{m_1}(c_\beta(z_1 T_{11} + z_2 T_{12}) + z_2 T_{22}s_\beta)\left(c_{23}s_{12} + c_{12}e^{-i\delta}s_{13}s_{23}\right)}{\sqrt{2f}\sqrt{\omega_1}} \\
&\quad - e^{-i(\eta_2+\eta_3)}\frac{e^{i\eta_3}\sqrt{m_2}\,T_{11}c_\beta\left(c_{12}c_{23} - e^{-i\delta}s_{12}s_{13}s_{23}\right) + c_{13}e^{i\eta_2}\sqrt{m_3}s_{23}(T_{22}s_\beta + T_{12}c_\beta)}{\sqrt{2f}\sqrt{\omega_1}},
\end{aligned}
\tag{42}
$$

$$
\begin{aligned}
Y^L_{31} &= e^{-i(\eta_2+\eta_3)}\frac{e^{i\eta_2}c_{13}c_{23}\sqrt{m_3}\,(T_{22}s_\beta + T_{12}c_\beta)}{\sqrt{2f}\sqrt{\omega_1}} \\
&\quad + \frac{\sqrt{m_1}(z_1 T_{11}c_\beta + z_2 T_{22}s_\beta + z_2 T_{12}c_\beta)\left(s_{12}s_{23} - c_{12}c_{23}e^{-i\delta}s_{13}\right)}{\sqrt{2f}\sqrt{\omega_1}} \\
&\quad + e^{-i(\eta_2+\eta_3)}\frac{-e^{i\eta_3}\sqrt{m_2}\,T_{11}c_\beta\left(c_{23}e^{-i\delta}s_{12}s_{13} + c_{12}s_{23}\right)}{\sqrt{2f}\sqrt{\omega_1}},
\end{aligned}
\tag{43}
$$

$$
\begin{aligned}
Y^L_{12} &= e^{-i(\eta_2+\eta_3)}\frac{e^{i\eta_2}T_{22}c_\beta^*\left(c_{12}c_{13}e^{i\eta_3}\sqrt{m_1}z_2 + e^{i\delta}\sqrt{m_3}s_{13}\right)}{\sqrt{2f}\sqrt{\omega_2}} \\
&\quad - e^{-i(\eta_2+\eta_3)}\frac{s_\beta^*\left(c_{13}e^{i\eta_3}\left(\sqrt{m_2}s_{12}T_{11} + c_{12}e^{i\eta_2}\sqrt{m_1}(z_1 T_{11} + z_2 T_{12})\right) + \sqrt{m_3}s_{13}T_{12}e^{i(\delta+\eta_2)}\right)}{\sqrt{2f}\sqrt{\omega_2}},
\end{aligned}
\tag{44}
$$

$$Y_{22}^L = \frac{\sqrt{m_1}\left(c_{23}s_{12} + c_{12}e^{-i\delta}s_{13}s_{23}\right)\left(s_\beta^*(z_1 T_{11} + z_2 T_{12}) - z_2 T_{22}c_\beta^*\right)}{\sqrt{2f}\sqrt{\omega_2}}$$

$$-e^{-i(\eta_2+\eta_3)}\frac{e^{i\eta_3}\sqrt{m_2}\,T_{11}s_\beta^*\left(c_{12}c_{23} - e^{-i\delta}s_{12}s_{13}s_{23}\right) - c_{13}e^{i\eta_2}\sqrt{m_3}s_{23}\left(T_{12}s_\beta^* - T_{22}c_\beta^*\right)}{\sqrt{2f}\sqrt{\omega_2}}, \tag{45}$$

$$Y_{32}^L = \frac{\sqrt{m_1}\left(c_{12}c_{23}e^{-i\delta}s_{13} - s_{12}s_{23}\right)\left(s_\beta^*(z_1 T_{11} + z_2 T_{12})z_2 T_{22}c_\beta^*\right)}{\sqrt{2f}\sqrt{\omega_2}}$$

$$+\frac{e^{-i\eta2}\sqrt{m_2}\,T_{11}s_\beta^*\left(c_{23}e^{-i\delta}s_{12}s_{13} + c_{12}s_{23}\right) - c_{13}c_{23}e^{-i\eta3}\sqrt{m_3}\left(T_{12}s_\beta^* - T_{22}c_\beta^*\right)}{\sqrt{2f}\sqrt{\omega_2}}, \tag{46}$$

$$Y_{11}^R = -e^{-i(\eta_2+\eta_3)}\frac{s_\beta^* c_{12}c_{13}\sqrt{m_1}e^{i(\eta_2+\eta_3)}(z_1 K_{12}T_{11} + z_2 K_{12}T_{12} - z_1 T_{12} + z_2 T_{11})}{\sqrt{2f}\sqrt{\omega_1}\,T_{11}T_{22}}$$

$$+e^{-i(\eta_2+\eta_3)}\frac{s_\beta^*\left(-c_{13}e^{i\eta_3}\sqrt{m_2}s_{12}(K_{12}T_{11} + T_{12}) + \sqrt{m_3}s_{13}e^{i(\delta+\eta_2)}(T_{11} - K_{12}T_{12})\right)}{\sqrt{2f}\sqrt{\omega_1}\,T_{11}T_{22}}$$

$$+e^{-i(\eta_2+\eta_3)}\frac{T_{22}c_\beta^*\left(c_{13}e^{i\eta_3}\left(\sqrt{m_2}s_{12} - c_{12}e^{i\eta_2}\sqrt{m_1}(z_1 - z_2 K_{12})\right) + \sqrt{m_3}s_{13}K_{12}e^{i(\delta+\eta_2)}\right)}{\sqrt{2f}\sqrt{\omega_1}\,T_{11}T_{22}}, \tag{47}$$

$$Y_{21}^R = \frac{s_\beta^*\sqrt{m_1}(z_1 K_{12}T_{11} + z_2 K_{12}T_{12} - z_1 T_{12} + z_2 T_{11})\left(c_{23}s_{12} + c_{12}e^{-i\delta}s_{13}s_{23}\right)}{\sqrt{2f}\sqrt{\omega_1}\,T_{11}T_{22}}$$

$$-e^{-i(\eta_2+\eta_3)}\frac{s_\beta^*\sqrt{m_1}\left(e^{i\eta_3}\sqrt{m_2}(K_{12}T_{11} + T_{12})\left(c_{12}c_{23} - e^{-i\delta}s_{12}s_{13}s_{23}\right) + c_{13}e^{i\eta_2}\sqrt{m_3}s_{23}(T_{11} - K_{12}T_{12})\right)}{\sqrt{2f}\sqrt{\omega_1}\,T_{11}T_{22}}$$

$$+e^{-i(\eta_2+\eta_3)}\frac{T_{22}c_\beta^*\left(\sqrt{m_1}e^{i(\eta_2+\eta_3)}(z_1 - z_2 K_{12})\left(c_{23}s_{12} + c_{12}e^{-i\delta}s_{13}s_{23}\right) + c_{13}e^{i\eta_2}\sqrt{m_3}s_{23}K_{12}\right)}{\sqrt{2f}\sqrt{\omega_1}\,T_{11}T_{22}}$$

$$+e^{-i(\eta_2+\eta_3)}\frac{T_{22}c_\beta^*\,e^{i\eta3}\sqrt{m_2}\left(c_{12}c_{23} - e^{-i\delta}s_{12}s_{13}s_{23}\right)}{\sqrt{2f}\sqrt{\omega_1}\,T_{11}T_{22}}, \tag{48}$$

$$Y_{31}^R = \frac{-\sqrt{m_1}\left(s_{12}s_{23} - c_{12}c_{23}e^{-i\delta}s_{13}\right)\left(s_\beta^*(T_{11}(z_1 K_{12} + z_2) - T_{12}(z_1 - z_2 K_{12}))\right)}{\sqrt{2f}\sqrt{\omega_1}\,T_{11}T_{22}}$$

$$-\frac{\sqrt{m_1}\left(s_{12}s_{23} - c_{12}c_{23}e^{-i\delta}s_{13}\right)T_{22}c_\beta^*(z_1 - z_2 K_{12})}{\sqrt{2f}\sqrt{\omega_1}\,T_{11}T_{22}}$$

$$+\frac{e^{-i\eta_2}\sqrt{m_2}\left((K_{12}T_{11} + T_{12})s_\beta^* - T_{22}c_\beta^*\right)\left(c_{23}e^{-i\delta}s_{12}s_{13} + c_{12}s_{23}\right)}{\sqrt{2f}\sqrt{\omega_1}\,T_{11}T_{22}}$$

$$+\frac{c_{13}c_{23}e^{-i\eta_3}\sqrt{m_3}\left((T_{11} - K_{12}T_{12})s_\beta^* + K_{12}T_{22}c_\beta^*\right)}{\sqrt{2f}\sqrt{\omega_1}\,T_{11}T_{22}}, \tag{49}$$

$$Y_{12}^R = -\frac{c_\beta c_{12}c_{13}\sqrt{m_1}(z_1 K_{12}T_{11} + z_2 K_{12}T_{12} - z_1 T_{12} + z_2 T_{11})}{\sqrt{2f}\sqrt{\omega_2}\,T_{11}T_{22}}$$

$$-e^{-i(\eta_2+\eta_3)}\frac{c_\beta\left(-c_{13}e^{i\eta_3}\sqrt{m_2}s_{12}(K_{12}T_{11} + T_{12}) + \sqrt{m_3}s_{13}e^{i(\delta+\eta_2)}(T_{11} - K_{12}T_{12})\right)}{\sqrt{2f}\sqrt{\omega_2}\,T_{11}T_{22}}$$

$$-e^{-i(\eta_2+\eta_3)}\frac{T_{22}s_\beta\left(c_{13}e^{i\eta_3}\left(\sqrt{m_2}s_{12} - c_{12}e^{i\eta_2}\sqrt{m_1}(z_1 - z_2 K_{12})\right) + \sqrt{m_3}s_{13}K_{12}e^{i(\delta+\eta_2)}\right)}{\sqrt{2f}\sqrt{\omega_2}\,T_{11}T_{22}}, \tag{50}$$

$$Y_{22}^R = \frac{\sqrt{m_1}\left(c_{23}s_{12} + c_{12}e^{-i\delta}s_{13}s_{23}\right)\left(T_{22}s_\beta(z_2K_{12} - z_1) + c_\beta(z_1K_{12}T_{11} + z_2K_{12}T_{12} - z_1T_{12} + z_2T_{11})\right)}{\sqrt{2}f\sqrt{\omega_2}\,T_{11}T_{22}}$$

$$-e^{-i(\eta_2+\eta_3)}\frac{e^{i\eta_3}\sqrt{m_2}(c_\beta(K_{12}T_{11} + T_{12}) + T_{22}s_\beta)\left(c_{12}c_{23} - e^{-i\delta}s_{12}s_{13}s_{23}\right)}{\sqrt{2}f\sqrt{\omega_2}\,T_{11}T_{22}}$$

$$+e^{-i(\eta_2+\eta_3)}\frac{c_{13}e^{i\eta_2}\sqrt{m_3}s_{23}(c_\beta(T_{11} - K_{12}T_{12}) - K_{12}T_{22}s_\beta)}{\sqrt{2}f\sqrt{\omega_2}\,T_{11}T_{22}}, \tag{51}$$

$$Y_{32}^R = \frac{-\sqrt{m_1}\left(s_{12}s_{23} - c_{12}c_{23}e^{-i\delta}s_{13}\right)\left(T_{22}s_\beta(z_2K_{12} - z_1) + c_\beta(z_1K_{12}T_{11} + z_2K_{12}T_{12} - z_1T_{12} + z_2T_{11})\right)}{\sqrt{2}f\sqrt{\omega_2}\,T_{11}T_{22}}$$

$$+e^{-i(\eta_2+\eta_3)}\frac{e^{i\eta_3}\sqrt{m_2}(c_\beta(K_{12}T_{11} + T_{12}) + T_{22}s_\beta)}{\sqrt{2}f\sqrt{\omega_2}\,T_{11}T_{22}}$$

$$+e^{-i(\eta_2+\eta_3)}\frac{\left(c_{23}e^{-i\delta}s_{12}s_{13} + c_{12}s_{23}\right) + c_{13}c_{23}e^{i\eta_2}\sqrt{m_3}(c_\beta(T_{11} - K_{12}T_{12}) - K_{12}T_{22}s_\beta)}{\sqrt{2}f\sqrt{\omega_2}\,T_{11}T_{22}}. \tag{52}$$

In these expressions $c_{kl} \equiv \cos\theta_{kl}$ and $s_{kl} \equiv \sin\theta_{kl}$ ($k = 1, 2$ and $l = 2, 3$; $l \neq k$) are the usual neutrino mixing angles measured in oscillation experiments, while $m_j \equiv \sqrt{m_1^2 + \Delta m_{j1}^2}$ ($j = 2, 3$) are neutrino mass eigenvalues. Moreover, m_1 is the lightest neutrino mass, η_i ($i = 2, 3$) are CP violating Majorana phases and δ is the CP violating Dirac phase. We also use the notation $s_\beta \equiv \sin\beta$ and $c_\beta \equiv \cos\beta$. In our numerical scans we have fixed $T_{11} = T_{22} = 1$ and $\beta = T_{12} = K_{12} = z_1 = z_2 = m_1 = \eta_i = \delta = 0$ unless otherwise stated.

References

1. A. Zee, A theory of lepton number violation, neutrino majorana mass, and oscillation. Phys. Lett. B **93**, 389 (1980). https://doi.org/10.1016/0370-2693(80)90349-4 (**Erratum: Phys. Lett. B 95, 461 (1980)**)
2. T.P. Cheng, L.-F. Li, Neutrino masses, mixings and oscillations in SU(2) × U(1) models of electroweak interactions. Phys. Rev. D **22**, 2860 (1980). https://doi.org/10.1103/PhysRevD.22.2860
3. A. Zee, Quantum numbers of Majorana Neutrino masses. Nucl. Phys. B **264**, 99–110 (1986). https://doi.org/10.1016/0550-3213(86)90475-X
4. K.S. Babu, Model of 'Calculable' Majorana Neutrino masses. Phys. Lett. B **203**, 132–136 (1988). https://doi.org/10.1016/0370-2693(88)91584-5
5. Y. Cai, J. Herrero-García, M.A. Schmidt, A. Vicente, R.R. Volkas, From the trees to the forest: a review of radiative neutrino mass models. Front. Phys. **5**, 63 (2017). https://doi.org/10.3389/fphy.2017.00063. arXiv:1706.08524 [hep-ph]
6. L.M. Krauss, S. Nasri, M. Trodden, A Model for neutrino masses and dark matter. Phys. Rev. D **67**, 085002 (2003). https://doi.org/10.1103/PhysRevD.67.085002. arXiv:hep-ph/0210389
7. D. Restrepo, O. Zapata, C.E. Yaguna, Models with radiative neutrino masses and viable dark matter candidates. JHEP **11**, 011 (2013). https://doi.org/10.1007/JHEP11(2013)011. arXiv:1308.3655 [hep-ph]
8. E. Ma, Verifiable radiative seesaw mechanism of neutrino mass and dark matter. Phys. Rev. D **73**, 077301 (2006). https://doi.org/10.1103/PhysRevD.73.077301. arXiv:hep-ph/0601225
9. T. Toma, A. Vicente, Lepton flavor violation in the Scotogenic model. JHEP **01**, 160 (2014). https://doi.org/10.1007/JHEP01(2014)160. arXiv:1312.2840 [hep-ph]
10. A. Vicente, C.E. Yaguna, Probing the scotogenic model with lepton flavor violating processes. JHEP **02**, 144 (2015). https://doi.org/10.1007/JHEP02(2015)144 arXiv:1412.2545 [hep-ph]
11. J. Kubo, E. Ma, D. Suematsu, Cold dark matter, radiative neutrino mass, $\mu \to e\gamma$, and Neutrinoless Double Beta Decay. Phys. Lett. B **642**, 18–23 (2006). https://doi.org/10.1016/j.physletb.2006.08.085. arXiv:hep-ph/0604114
12. D.A. Sierra, J. Kubo, D. Restrepo, D. Suematsu, O. Zapata, Radiative seesaw: warm dark matter, collider and lepton flavour violating signals. Phys. Rev. D **79**, 013011 (2009). https://doi.org/10.1103/PhysRevD.79.013011. arXiv:0808.3340 [hep-ph]
13. D. Suematsu, T. Toma, T. Yoshida, Reconciliation of CDM abundance and $\mu \to e\gamma$ in a radiative seesaw model. Phys. Rev. D **79**, 093004 (2009). https://doi.org/10.1103/PhysRevD.79.093004. arXiv:0903.0287 [hep-ph]
14. A. Adulpravitchai, M. Lindner, A. Merle, Confronting flavour symmetries and extended scalar sectors with lepton flavour violation bounds. Phys. Rev. D **80**, 055031 (2009). https://doi.org/10.1103/PhysRevD.80.055031. arXiv:0907.2147 [hep-ph]
15. C. Hagedorn, J. Herrero-García, E. Molinaro, M.A. Schmidt, Phenomenology of the generalised scotogenic model with fermionic dark matter. JHEP **11**, 103 (2018). https://doi.org/10.1007/JHEP11(2018)103. arXiv:1804.04117 [hep-ph]
16. N.G. Deshpande, E. Ma, Pattern of symmetry breaking with two Higgs doublets. Phys. Rev. D **18**, 2574 (1978). https://doi.org/10.1103/PhysRevD.18.2574
17. R. Barbieri, L.J. Hall, V.S. Rychkov, Improved naturalness with a heavy Higgs: an alternative road to LHC physics. Phys. Rev. D **74**, 015007 (2006). https://doi.org/10.1103/PhysRevD.74.015007. arXiv:hep-ph/0603188
18. L. Lopez Honorez, E. Nezri, J.F. Oliver, M.H.G. Tytgat, The inert doublet model: an archetype for dark matter. JCAP **02**, 028 (2007). https://doi.org/10.1088/1475-7516/2007/02/028. arXiv:hep-ph/0612275
19. L. Lopez Honorez, C.E. Yaguna, The inert doublet model of dark matter revisited. JHEP **09**, 046 (2010). https://doi.org/10.1007/JHEP09(2010)046. arXiv:1003.3125 [hep-ph]

20. M.A. Díaz, B. Koch, S. Urrutia-Quiroga, Constraints to dark matter from inert Higgs doublet model. Adv. High Energy Phys. **2016**, 8278375 (2016). https://doi.org/10.1155/2016/8278375. arXiv:1511.04429 [hep-ph]

21. P. Escribano, M. Reig, A. Vicente, Generalizing the Scotogenic model. JHEP **07**, 097 (2020). https://doi.org/10.1007/JHEP07(2020)097. arXiv:2004.05172 [hep-ph]

22. E. Ma, V. De Romeri, Radiative seesaw dark matter. arXiv:2105.00552 [hep-ph]

23. M. Hirsch, R.A. Lineros, S. Morisi, J. Palacio, N. Rojas, J.W.F. Valle, WIMP dark matter as radiative neutrino mass messenger. JHEP **10**, 149 (2013). https://doi.org/10.1007/JHEP10(2013)149 arXiv:1307.8134 [hep-ph]

24. P. Rocha-Moran, A. Vicente, Lepton flavor violation in the singlet-triplet scotogenic model. JHEP **07**, 078 (2016). https://doi.org/10.1007/JHEP07(2016)078 arXiv:1605.01915 [hep-ph]

25. I.M. Ávila, V. De Romeri, L. Duarte, J.W.F. Valle, Phenomenology of scotogenic scalar dark matter. Eur. Phys. J. C **80**(10), 908 (2020). https://doi.org/10.1140/epjc/s10052-020-08480-z arXiv:1910.08422 [hep-ph]

26. M. Aoki, S. Kanemura, K. Yagyu, Doubly-charged scalar bosons from the doublet, Phys. Lett. B **702**, 355–358 (2011). https://doi.org/10.1016/j.physletb.2011.07.017. arXiv:1105.2075 [hep-ph] (**Erratum: Phys.Lett.B 706, 495–495 (2012)**)

27. K. Enomoto, S. Kanemura, K. Katayama, Probing doubly charged scalar bosons from the doublet at future high-energy colliders. Phys. Rev. D **104**(3), 035040 (2021). https://doi.org/10.1103/PhysRevD.104.035040 arXiv:2102.12950 [hep-ph]

28. D. Binosi, L. Theussl, JaxoDraw: a graphical user interface for drawing Feynman diagrams. Comput. Phys. Commun. **161**, 76–86 (2004). https://doi.org/10.1016/j.cpc.2004.05.001 arXiv:hep-ph/0309015

29. D. Binosi, J. Collins, C. Kaufhold, L. Theussl, JaxoDraw: a graphical user interface for drawing Feynman diagrams. Version 2.0 release notes. Comput. Phys. Commun. **180**, 1709–1715 (2009). https://doi.org/10.1016/j.cpc.2009.02.020 arXiv:0811.4113 [hep-ph]

30. G.'t Hooft, Naturalness, chiral symmetry, and spontaneous chiral symmetry breaking. NATO Sci. Ser. B **59**, 135–157 (1980). https://doi.org/10.1007/978-1-4684-7571-5_9

31. F. Staub, SARAH 4: A tool for (not only SUSY) model builders. Comput. Phys. Commun. **185**, 1773–1790 (2014). https://doi.org/10.1016/j.cpc.2014.02.018 arXiv:1309.7223 [hep-ph]

32. A. Vicente, Computer tools in particle physics. arXiv:1507.06349 [hep-ph]

33. W. Porod, SPheno, a program for calculating supersymmetric spectra, SUSY particle decays and SUSY particle production at e+ e- colliders. Comput. Phys. Commun. **153**, 275–315 (2003). https://doi.org/10.1016/S0010-4655(03)00222-4 arXiv:hep-ph/0301101

34. W. Porod, F. Staub, SPheno 3.1: extensions including flavour, CP-phases and models beyond the MSSM. Comput. Phys. Commun. **183**, 2458–2469 (2012). https://doi.org/10.1016/j.cpc.2012.05.021 arXiv:1104.1573 [hep-ph]

35. W. Porod, F. Staub, A. Vicente, A Flavor Kit for BSM models. Eur. Phys. J. C **74**(8), 2992 (2014). https://doi.org/10.1140/epjc/s10052-014-2992-2 arXiv:1405.1434 [hep-ph]

36. G. Bélanger, F. Boudjema, A. Goudelis, A. Pukhov, B. Zaldivar, micrOMEGAs5.0: Freeze-in. Comput. Phys. Commun. **231**, 173–186 (2018). https://doi.org/10.1016/j.cpc.2018.04.027 arXiv:1801.03509 [hep-ph]

37. P.F. de Salas, D.V. Forero, S. Gariazzo, P. Martínez-Miravé, O. Mena, C.A. Ternes, M. Tórtola, J.W.F. Valle, 2020 global reassessment of the neutrino oscillation picture. JHEP **02**, 071 (2021). https://doi.org/10.1007/JHEP02(2021)071 arXiv:2006.11237 [hep-ph]

38. I. Cordero-Carrión, M. Hirsch, A. Vicente, Master Majorana neutrino mass parametrization. Phys. Rev. D **99**(7), 075019 (2019). https://doi.org/10.1103/PhysRevD.99.075019 arXiv:1812.03896 [hep-ph]

39. I. Cordero-Carrión, M. Hirsch, A. Vicente, General parametrization of Majorana neutrino mass models. Phys. Rev. D **101**(7), 075032 (2020). https://doi.org/10.1103/PhysRevD.101.075032 arXiv:1912.08858 [hep-ph]

40. M.E.G. Collaboration, A.M. Baldini et al., Search for the lepton flavour violating decay $\mu^+ \to e^+\gamma$ with the full dataset of the MEG experiment. Eur. Phys. J. C **76**(8), 434 (2016). https://doi.org/10.1140/epjc/s10052-016-4271-x arXiv:1605.05081 [hep-ex]

41. SINDRUM Collaboration, U. Bellgardt et al., Search for the Decay $\mu^+ \to e^+e^+e^-$. Nucl. Phys. B **299**, 1–6 (1988). https://doi.org/10.1016/0550-3213(88)90462-2

42. SINDRUM II Collaboration, W.H. Bertl et al., A Search for muon to electron conversion in muonic gold. Eur. Phys. J. C **47**, 337–346 (2006). https://doi.org/10.1140/epjc/s2006-02582-x

43. Particle Data Group Collaboration, P.A. Zyla et al., Review of Particle Physics. PTEP **2020**(8), 083C01 (2020). https://doi.org/10.1093/ptep/ptaa104

44. Planck Collaboration, N. Aghanim et al., Planck 2018 results. VI. Cosmological parameters. Astron. Astrophys. **641**, A6 (2020). https://doi.org/10.1051/0004-6361/201833910. arXiv:1807.06209 [astro-ph.CO]

45. XENON Collaboration, E. Aprile et al., Dark Matter Search Results from a One Ton-Year Exposure of XENON1T. Phys. Rev. Lett. **121**(11), 111302 (2018). https://doi.org/10.1103/PhysRevLett.121.111302. arXiv:1805.12562 [astro-ph.CO]

46. M. Klasen, C.E. Yaguna, J.D. Ruiz-Alvarez, Electroweak corrections to the direct detection cross section of inert Higgs dark matter. Phys. Rev. D **87**, 075025 (2013). https://doi.org/10.1103/PhysRevD.87.075025 arXiv:1302.1657 [hep-ph]

47. Fermi-LAT Collaboration, M. Ackermann et al., Searching for dark matter annihilation from milky way dwarf spheroidal galaxies with six years of fermi large area telescope data. Phys. Rev. Lett. **115**(23), 231301 (2015). https://doi.org/10.1103/PhysRevLett.115.231301. arXiv:1503.02641 [astro-ph.HE]

48. H.E.S.S. Collaboration, H. Abdallah et al., Search for dark matter annihilations towards the inner Galactic halo from 10 years of observations with H.E.S.S. Phys. Rev. Lett. **117**(11), 111301 (2016). https://doi.org/10.1103/PhysRevLett.117.111301. arXiv:1607.08142 [astro-ph.HE]

49. AMS Collaboration, M. Aguilar et al., Antiproton flux, antiproton-to-proton flux ratio, and properties of elementary particle fluxes in primary cosmic rays measured with the alpha magnetic spectrometer on the international space station. Phys. Rev. Lett. **117**(9), 091103 (2016). https://doi.org/10.1103/PhysRevLett.117.091103

50. A. Reinert, M.W. Winkler, A precision search for WIMPs with charged cosmic rays. JCAP **01**, 055 (2018). https://doi.org/10.1088/1475-7516/2018/01/055 arXiv:1712.00002 [astro-ph.HE]

51. A. Cuoco, J. Heisig, M. Korsmeier, M. Krämer, Constraining heavy dark matter with cosmic-ray antiprotons. JCAP **04**, 004 (2018). https://doi.org/10.1088/1475-7516/2018/04/004 arXiv:1711.05274 [hep-ph]

52. ATLAS Collaboration, M. Aaboud et al., Search for doubly charged scalar bosons decaying into same-sign W boson pairs with the ATLAS detector. Eur. Phys. J. C **79**(1), 58 (2019). https://doi.org/10.1140/epjc/s10052-018-6500-y. arXiv:1808.01899 [hep-ex]

53. ATLAS Collaboration, M. Aaboud et al., Search for doubly charged Higgs boson production in multi-lepton final states with the ATLAS detector using proton–proton collisions at $\sqrt{s} = 13$ TeV. Eur. Phys. J. C **78**(3), 199 (2018). https://doi.org/10.1140/epjc/s10052-018-5661-z. arXiv:1710.09748 [hep-ex]

54. CMS Collaboration, A.M. Sirunyan et al., Search for invisible decays of a Higgs boson produced through vector boson fusion

in proton–proton collisions at $\sqrt{s} = 13$ TeV. Phys. Lett. B **793**, 520–551 (2019). https://doi.org/10.1016/j.physletb.2019.04.025. arXiv:1809.05937 [hep-ex]

55. LUX Collaboration, D. Akerib et al., Results from a search for dark matter in the complete LUX exposure. Phys. Rev. Lett. **118**(2), 021303 (2017). https://doi.org/10.1103/PhysRevLett.118.021303. arXiv:1608.07648 [astro-ph.CO]

56. LUX Collaboration, D.S. Akerib et al., Results of a Search for Sub-GeV Dark Matter Using 2013 LUX Data. Phys. Rev. Lett. **122**(13), 131301 (2019). https://doi.org/10.1103/PhysRevLett.122.131301. arXiv:1811.11241 [astro-ph.CO]

57. PandaX-II Collaboration, X. Cui et al., Dark matter results from 54-ton-day exposure of PandaX-II experiment. Phys. Rev. Lett. **119**(18), 181302 (2017). https://doi.org/10.1103/PhysRevLett.119.181302. arXiv:1708.06917 [astro-ph.CO]

58. DarkSide Collaboration, P. Agnes et al., DarkSide-50 532-day dark matter search with low-radioactivity argon. Phys. Rev. D **98**(10), 102006 (2018). https://doi.org/10.1103/PhysRevD.98.102006. arXiv:1802.07198 [astro-ph.CO]

59. D.E.A.P. Collaboration, R. Ajaj et al., Search for dark matter with a 231-day exposure of liquid argon using DEAP-3600 at SNO-LAB. Phys. Rev. D **100**(2), 022004 (2019). https://doi.org/10.1103/PhysRevD.100.022004 arXiv:1902.04048 [astro-ph.CO]

60. J. Billard, L. Strigari, E. Figueroa-Feliciano, Implication of neutrino backgrounds on the reach of next generation dark matter direct detection experiments. Phys. Rev. D **89**(2), 023524 (2014). https://doi.org/10.1103/PhysRevD.89.023524 arXiv:1307.5458 [hep-ph]

61. LUX-ZEPLIN Collaboration, D.S. Akerib et al., Projected WIMP sensitivity of the LUX-ZEPLIN dark matter experiment. Phys. Rev. D **101**(5), 052002 (2020). https://doi.org/10.1103/PhysRevD.101.052002. arXiv:1802.06039 [astro-ph.IM]

62. XENON Collaboration, E. Aprile et al., Projected WIMP sensitivity of the XENONnT dark matter experiment. JCAP **11**, 031 (2020). https://doi.org/10.1088/1475-7516/2020/11/031. arXiv:2007.08796 [physics.ins-det]

63. GADMC Collaboration, C. Galbiati et al., Future dark matter searches with low-radioactivity argon, Input to the European Particle Physics Strategy Update 2018–2020 (2018) . https://indico.cern.ch/event/765096/contributions/3295671/attachments/1785196/2906164/DarkSide-Argo_ESPP_Dec_17_2017.pdf

64. M. Schumann et al., Dark matter sensitivity of multi-ton liquid xenon detectors. JCAP **1510**(10), 016 (2015). https://doi.org/10.1088/1475-7516/2015/10/016 arXiv:1506.08309 [physics.ins-det]

65. DARWIN Collaboration, J. Aalbers et al., DARWIN: towards the ultimate dark matter detector. JCAP **1611**, 017 (2016). https://doi.org/10.1088/1475-7516/2016/11/017. arXiv:1606.07001 [astro-ph.IM]

66. J. Billard et al., Direct Detection of Dark Matter-APPEC Committee Report. arXiv:2104.07634 [hep-ex]

67. C. Garcia-Cely, A. Ibarra, Novel gamma-ray spectral features in the inert doublet model. JCAP **09**, 025 (2013). https://doi.org/10.1088/1475-7516/2013/09/025 arXiv:1306.4681 [hep-ph]

68. F. Giacchino, L. Lopez-Honorez, M.H.G. Tytgat, Scalar dark matter models with significant internal bremsstrahlung. JCAP **10**, 025 (2013). https://doi.org/10.1088/1475-7516/2013/10/025 arXiv:1307.6480 [hep-ph]

69. PAMELA Collaboration, O. Adriani et al., An anomalous positron abundance in cosmic rays with energies 1.5-100 GeV. Nature **458**, 607–609 (2009). https://doi.org/10.1038/nature07942. arXiv:0810.4995 [astro-ph]

70. PAMELA Collaboration, O. Adriani et al., Cosmic-ray positron energy spectrum measured by PAMELA. Phys. Rev. Lett. **111**, 081102 (2013). https://doi.org/10.1103/PhysRevLett.111.081102. arXiv:1308.0133 [astro-ph.HE]

71. AMS Collaboration, L. Accardo et al., High statistics measurement of the positron fraction in primary cosmic rays of 0.5–500 GeV with the alpha magnetic spectrometer on the international space station. Phys. Rev. Lett. **113**, 121101 (2014) . https://doi.org/10.1103/PhysRevLett.113.121101

72. A.M.S. Collaboration, M. Aguilar et al., Towards understanding the origin of cosmic-ray positrons. Phys. Rev. Lett. **122**(4), 041102 (2019). https://doi.org/10.1103/PhysRevLett.122.041102

73. A. Cuoco, J. Heisig, L. Klamt, M. Korsmeier, M. Krämer, Scrutinizing the evidence for dark matter in cosmic-ray antiprotons. Phys. Rev. D **99**(10), 103014 (2019). https://doi.org/10.1103/PhysRevD.99.103014 arXiv:1903.01472 [astro-ph.HE]

74. I. Cholis, T. Linden, D. Hooper, A robust excess in the cosmic-ray antiproton spectrum: implications for annihilating dark matter. Phys. Rev. D **99**(10), 103026 (2019). https://doi.org/10.1103/PhysRevD.99.103026 arXiv:1903.02549 [astro-ph.HE]

75. J. Heisig, M. Korsmeier, M.W. Winkler, Dark matter or correlated errors: systematics of the AMS-02 antiproton excess. Phys. Rev. Res. **2**(4), 043017 (2020). https://doi.org/10.1103/PhysRevResearch.2.043017 arXiv:2005.04237 [astro-ph.HE]

76. Fermi-LAT Collaboration, E. Charles et al., Sensitivity projections for dark matter searches with the fermi large area telescope. Phys. Rep. **636**, 1–46 (2016). https://doi.org/10.1016/j.physrep.2016.05.001. arXiv:1605.02016 [astro-ph.HE]

77. CTA Consortium Collaboration, B.S. Acharya et al., Science with the Cherenkov Telescope Array. WSP, 11 (2018). https://doi.org/10.1142/10986. arXiv:1709.07997 [astro-ph.IM]

78. A. Sommerfeld, Über die Beugung und Bremsung der Elektronen. Ann. Phys. **403**(3), 257–330 (1931). https://doi.org/10.1002/andp.19314030302

79. J. Hisano, S. Matsumoto, M.M. Nojiri, Explosive dark matter annihilation. Phys. Rev. Lett. **92**, 031303 (2004). https://doi.org/10.1103/PhysRevLett.92.031303 arXiv:hep-ph/0307216

80. J. Hisano, S. Matsumoto, M.M. Nojiri, O. Saito, Non-perturbative effect on dark matter annihilation and gamma ray signature from galactic center. Phys. Rev. D **71**, 063528 (2005). https://doi.org/10.1103/PhysRevD.71.063528 arXiv:hep-ph/0412403

81. N. Arkani-Hamed, D.P. Finkbeiner, T.R. Slatyer, N. Weiner, A theory of dark matter. Phys. Rev. D **79**, 015014 (2009). https://doi.org/10.1103/PhysRevD.79.015014 arXiv:0810.0713 [hep-ph]

82. T.A. Chowdhury, S. Nasri, The sommerfeld enhancement in the scotogenic model with large electroweak scalar multiplets. JCAP **01**, 041 (2017). https://doi.org/10.1088/1475-7516/2017/01/041 arXiv:1611.06590 [hep-ph]

83. A. Merle, M. Platscher, Parity problem of the scotogenic neutrino model. Phys. Rev. D **92**(9), 095002 (2015). https://doi.org/10.1103/PhysRevD.92.095002 arXiv:1502.03098 [hep-ph]